J. Appl. Comput. Mech., 12(1) (2026) 21-30
DOI: 10.22055/jacm.2025.48157.5019

ISSN: 2383-4536
jacm.scu.ac.ir

Shahid Chamran University of Ahvaz

Journal of
Applied and Computational Mechanics

Research Paper

Numerical Investigation of Double Low-Velocity Impact and Post-Impact Compression Behavior in Laminated Composites

Khairul Anam[1], **Melanie Todt**[2], **Heinz E. Pettermann**[2]

[1] Department of Mechanical Engineering, Brawijaya University, Jl. MT Haryono 167, Malang 65145, Indonesia, Email: khairul.anam27@ub.ac.id

[2] Institute of Lightweight Design and Structural Biomechanics, TU Wien, Getreidemarkt 9, 1060 Vienna, Austria,
Email: melanie.todt@tuwien.ac.at (M.T.); heinz.pettermann@tuwien.ac.at (H.E.P.)

Received January 17 2025; Revised March 06 2025; Accepted for publication March 07 2025.
Corresponding author: K. Anam (khairul.anam27@ub.ac.id)

Abstract. Low-velocity impact can significantly reduce the structural integrity of the laminated composites, and it can be exacerbating the damage if it occurs repeatedly. In this study, double low-velocity impacts are numerically applied on the laminates by utilizing ply-level based modeling strategy, which each ply and each interface of the laminate is explicitly modeled, with the plies represented by conventional shell elements and the interfaces are discretized using cohesive zone elements. The impact results are then directly utilized to predict the residual compressive strength of the laminates by performing compression after impact simulation. Furthermore, the impact responses and the structural integrity of the laminated composites are compared for all configurations including single and double impact events for various distances. The numerical results show that in the double 0 mm case, the second impactor experiences significantly higher displacement due to reduced transverse shear stiffness from the first impact. The double 10 mm configuration exhibits the largest delamination growth, leading to the most severe compressive strength reduction from 634 MPa to 311 MPa. Additionally, the results show that the distance between two impact positions provides different delamination interference mechanisms which are consistent with the previous experimental findings. Overall, the results provide quantitative insights into damage mechanisms, delamination growth, and residual strength reduction, which are crucial for designing more impact-resistant composite structures. Meanwhile, the implementation of a ply-level-based modeling strategy ensures high computational efficiency in predicting impact responses and compressive strength in laminated composite structures.

Keywords: Laminates, Delamination, Finite element analysis (FEA), Double impact position, Damage characteristic.

1. Introduction

Laminated composites are increasingly being used in the aircraft industry due to their outstanding mechanical characteristics such as high stiffness and strength to weight ratios which are important characteristics for lightweight design [1]. Furthermore, these materials have good fatigue performance, high corrosion resistivity, and are easily formed during manufacturing processes. However, laminated composites are susceptible to impact damage due to the weak transverse load-carrying capacity [2]. Impact loading of laminated composites can induce complex damage mechanisms, including matrix cracking, fiber breakage, plastic deformation, and delamination [3-6]. Such damage must be considered in the design and maintenance phase of composite aircraft structures [7-9]. Therefore, investigating the damage mechanisms of laminated composites under impact loading conditions is an important consideration in order to increase the impact resistance and the residual strength after impact of laminated composite structures.

Impact loading of laminated composites is generally classified into low, intermediate, high/ballistic, and hyper velocity regimes, as they will lead to different damage mechanisms and failure behavior [10]. Between four different velocities, low-velocity impact (LVI) testing is frequently performed to investigate the composite damage tolerance in order to improve the lightweight design of laminated composite structures. In aircraft applications, LVI damage is not only caused by operational activities such as hailstone strikes and runway debris but also by maintenance and service activities including part movement and incidental tool drops. Consequently, laminated composite structures are usually exposed to complex multiple impact environments [11-13]. Thus, understanding the damage mechanisms and failure behavior of laminated composites under multiple LVIs is important. Furthermore, impact resistance and damage tolerance as two standard indicators have been created to measure the performance of composite materials under out-of-plane stresses [14-16]. The amount of absorbed energy and induced damage generated by a certain impact energy characterize the impact resistance of the composite material. The damage tolerance is defined as the ability to retain undamaged or original strength, which is assessed by evaluating residual strength after impact [16], particularly in compression. The residual compressive strength of impacted laminated composites is commonly obtained by performing compression after impact (CAI) experiments which are usually conducted with quasi static uniaxial compressive load. Multiple LVIs

Published online: March 26 2025

and CAI tests on laminated composites have been extensively done both experimentally and numerically over the last few decades. Andrew et al. [17] used an acoustic emission monitoring technique to evaluate the compressive damage process for repaired and unrepaired laminated glass fiber reinforced composites after repeated impacts at the same position. Liao et al. [13] investigated experimentally the effect of double LVI positions on impact response and damage interference mechanism for laminated composites. They revealed that the interference status for mechanical curves directly corresponded to the impact-induced damage modes at different impact energy. Moreover, for a double impact event at the same position, the maximum indentation of the second impactor is higher than the first one due to the decreasing bending stiffness caused by the first impact. Saleh et al. [15] investigated the residual compressive strength of laminated composites with different fabric architectures after repeated LVIs. They found that the residual strength of 3D woven composites is significantly higher than that of 2D plain woven specimens resulting in sudden catastrophic damage. Anuse et al. [18] have analyzed the residual compressive strength of carbon fiber reinforced composite laminates with different ply orientation sequences by using experimental and numerical methods. Three different energy levels have been studied to explore the LVI of laminated composites. They discovered that even with barely visible impact damages, the residual compressive strength of the laminated composites has been significantly decreased. Generally, the experimental procedure provides insight into the general impact behavior of the specimens under certain loading conditions. However, studying a variety of different loading scenarios is time consuming and costly. It is even more difficult to investigate the impact behavior and structural integrity of large-scale and complex structures. Meanwhile, numerical procedures provide capabilities to predict the nonlinear mechanical behavior including damage mechanisms and failure behavior of laminated composites under impact loading conditions at various length scales [19]. Still, for highly nonlinear mechanical responses due to impact loading, numerical methods need a high computational time. Therefore, an efficient modeling strategy must be used to accelerate the computational analyses while still providing reliable results. The focus of this paper is on the investigation of the failure and delamination behavior in laminated composites under LVI and CAI by performing a ply-level modeling strategy based on conventional shell elements in combination with finite geometrical thickness of cohesive zone element (CZE). Both LVI and CAI are simulated by using commercial FEM code Abaqus/Explicit 2020 (Dassault Systèmes Simulia Corp., Providence, RI, USA). Single and double LVI simulations are carried out on laminated composite plates. Three different impact distances between two impact positions are compared. For the LVI event, the impact energy is kept so low that the damage is dominated by delamination and no matrix cracking or fiber breaking occurs. CAI simulation is applied for all these impacted laminated composite plates, along with the unimpacted laminated composite plate to investigate the failure behavior and residual compressive strength of the laminated composites. The LVI and CAI simulations are done under ideal conditions and following ASTM standards D7136/D7136M and D7137/D7137M [20, 21]. The impact response, energy dissipation, delamination area, and delamination pattern are examined. The delamination pattern due to impact is then validated by comparing the with the experimental studies done by Liao et al. [13]. Furthermore, the structural integrity of the laminated composites is also examined in terms of stiffness degradation and compressive residual strength values. Finally, computation times are measured and compared with previous studies. Generally, this study provides quantitative insights into damage mechanisms, delamination growth, and residual strength reduction, which are essential for designing more impact-resistant composite structures. Meanwhile, the implementation of a ply-level-based modeling strategy ensures high computational efficiency in predicting impact responses and compressive strength in laminated composite structures.

2. Modeling Strategy

The modeling strategy is performing the ply-level modeling based on conventional shell element together with finite geometrical thickness of CZE by the means of Finite Element Method (FEM) since it has been found to be the most efficient compared to other ply-level based modeling [1]. The CZEs share the nodes of the adjacent shell elements which are positioned at the corresponding midplanes of plies as shown in Fig. 1. As a result, the thickness of the CZE is the same as the thickness of the corresponding plies. While the CZEs have a finite geometrical thickness, they are able to effectively represent the behavior of an infinitely thin interface [5]. The interface constitutive response is modelled using the Abaqus built-in traction-separation based constitutive model for CZEs [22].

Individual constitutive laws for plies and interfaces are employed to account for the appropriate damage and failure mechanisms such as intra- and inter-ply, respectively, for both damage initiation and propagation. Intra-ply damage and failure of the plies are accounted for tensile and compressive fiber damage as well as matrix cracking by an energy-based continuum damage mechanics approach of the Hashin damage criterion [22-26]. Moreover, the damage is modeled under shear loading to capture the ply's behavior where the matrix plays an important role in resisting shear forces. It has to be noted that intra-ply damage and failure are mainly considered during CAI analysis since low impact energy of the LVI event is unlikely to cause matrix cracking or fiber breakage.

Inter-ply failure such as delamination is modeled by cohesive zone elements using a bilinear traction-separation based constitutive law, cf. [27]. Damage initiation of the CZEs is expected to occur when a quadratic interaction function with nominal stress ratios reaches a value of one [26]. This criterion is expressed as follows:

$$\left\{\frac{\langle t_\mathrm{n}\rangle}{t_\mathrm{n}^0}\right\}^2 + \left\{\frac{t_\mathrm{s}}{t_\mathrm{s}^0}\right\}^2 + \left\{\frac{t_\mathrm{t}}{t_\mathrm{t}^0}\right\}^2 \geq 1 \tag{1}$$

where, t_i are the normal, *n*, shear, *s* and transverse, *t*, component of the traction vector and t_i^0 are the corresponding interlaminar strengths. Damage evolution is modeled based on the critical energy release rates in combination with a linear softening law.

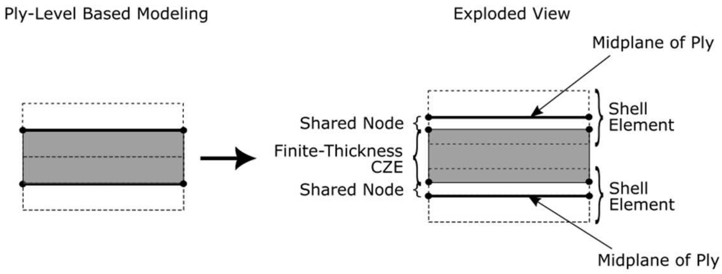

Fig. 1. Exploded view of the coupling strategy between finite thickness of cohesive zone element and the adjacent shell elements [1].

The Benzeggagh and Kenane (BK) criterion is used to treat the mixed mode behavior [28], which is based on different energies and is given by:

$$\mathcal{G}^C = \mathcal{G}_n^C + (\mathcal{G}_s^C - \mathcal{G}_n^C)(B)^\eta \tag{2}$$

$$B = \frac{\mathcal{G}_s + \mathcal{G}_t}{\mathcal{G}_n + \mathcal{G}_s + \mathcal{G}_t} \tag{3}$$

where, $\mathcal{G}_i^C$ are the fracture toughness values, B is the mode-mixity, and $\mathcal{G}_i$ describe the work done by the pure mode tractions t_i on the corresponding separations δ_i, and η is a mixed mode parameter obtained from experiments. In this study, the mixed mode parameter, $\eta = 2$ is selected [27].

A contact definition between the plies needs to be employed to avoid overclosures in delamination zones [26] in which CZEs are deleted due to impact. This additional contact is enforced using the Abaqus/Explicit general contact by scaling the surface thickness of the plies by a factor of 0.8 which are utilized within the contact calculation.

3. Numerical Procedures

The described modeling strategy is implemented to investigate the damage mechanism and failure behavior of the laminated composite under LVI and CAI events by using FEM package Abaqus/Explicit. The explicit time integration approach is used to examine the highly nonlinear impact response of the laminated composite plates. A schematic illustration of the modeled setup is presented in Fig. 2 comprising (a) ply arrangement, (b) mesh visualization, (c) single LVI set up, (d) double LVI set up, and (e) CAI set up. Details will be provided in the following subsection.

3.1. Geometrical discretization

Figure 2(a) shows a sketch of the ply arrangement in the thickness direction. The laminate is modeled by applying the ply-level based modeling as described above. The laminates are composed of eight plies modeled by shell elements. The seven associated interfaces are modeled with finite thickness cohesive zone elements. Figure 2(b) shows the mesh visualization of the laminated composites as well as the spherical impactor. The ply element is a 4-nodal, linearly interpolated, and fully integrated conventional shell element. The integration in the thickness direction takes place via three integration points according to the Simpson rule. The normal direction of all shell layers points in the positive z-direction.

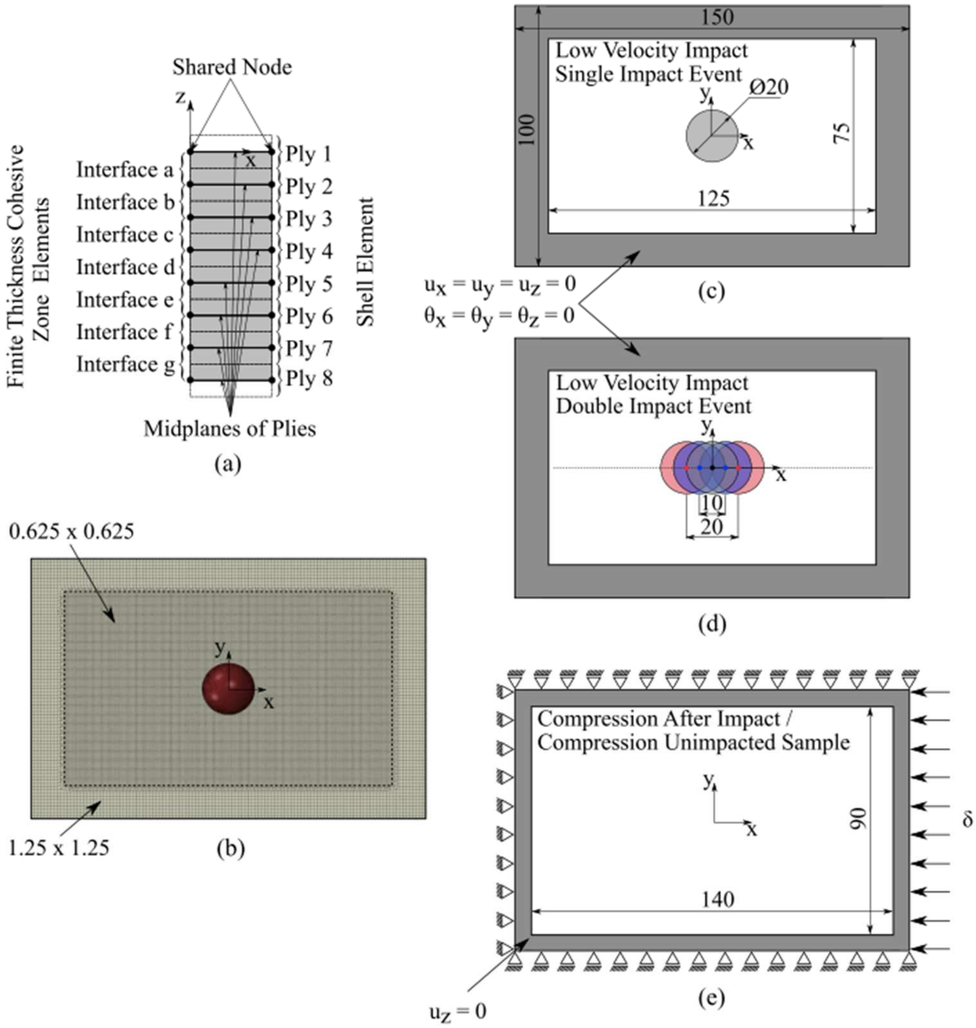

Fig. 2. A schematic illustration of the modeled setup (dimensions in mm) including (a) ply arrangement, (b) mesh visualization, (c) single LVI set up, (d) double LVI set up, and (e) CAI set up.

Laminated composites with the size of 150 mm × 100 mm are utilized according to ASTM standards. The LVI model uses an element size of 0.625 mm x 0.625 mm with an assigned thickness per ply of 0.5 mm. The element edges run parallel to the edges of the specimen panel. The plate area represented in gray regions in Figs. 2(c-e) is equipped with an element size of 1.25 mm x 1.25 mm modeled with constant shell thickness. Since the cohesive zone elements use the same nodes and thus have the same element size. The mesh size of the impactor is about 0.5 mm x 0.5 mm on the spherical surface. Additionally, the volume of the sphere is filled with volume elements including eight-node brick and six-node wedge elements. Generally, the model consists of 561,435 elements with a total of 255,370 nodes and 1,448,580 degrees of freedom (DOF).

The impactor is modeled as quasi-rigid body since the impactor can be approximated as a rigid body in comparison to the laminates [29]. In terms of impactor facet, a sharp shape generally leads to an increased number of fiber defects and large penetration. On the other hand, a flat shape causes higher momentum transfer to the laminated composite and thus causes large-scale delamination. With respect to the size of the impactor, small foreign bodies induce localized damage and a high penetration depth, large foreign bodies cause deformation of the entire structure and, as a result, cause greater interface damage [30,31]. With these two factors, a spherical impactor with a 20 mm diameter is chosen.

3.2. Boundary conditions

For the LVI simulation, a domain with a size of 125 mm × 75 mm × 4 mm is set as the impact site which is shown in the white region in Fig. 2(c). At the grey region, all translational and rotational DOFs are fixed. This is a simplification of the jig in the experimental set up to mimic a fixed clamping on the circumference of the plate. The impactor movement is fixed for all DOFs except for translational movement along the *z*-direction. The load introduction to the laminate is modeled by defining contact between the impactor and the top surfaces of the top ply. It has to be noted, that frictionless behavior is assumed for every contact definition. The impact loading is performed with an initial velocity of 4 m/s and a mass of 0.25 kg. Consequently, the impact energy of 2 J is completely determined for all configurations. At the end of the simulation, there are still a few nodes directly at the impact point in a slight swinging motion as a vibration effect of the impact loading. For this reason, all node velocities are set to zero at the beginning of the second LVI simulation and/or CAI simulation. At this time, the first impactor is already in an upward motion and, therefore, has no influence on the subsequent second LVI and/or CAI simulations. Moreover, three different positions of the double impact event including 0 mm, ± 10 mm, and ± 20 mm from the center of the laminates can be seen in Fig. 2(d).

For CAI simulation, new boundary conditions are now defined as illustrated in Fig. 2(e). At the top and bottom of the plate, the displacements in the *z*-direction are fixed within a range of 5 mm on the circumference of the plate to mimic anti buckling guides. At the two edges of the long side of the plate, the displacement of all nodes of the individual layers in the *y*-direction and at the left edge in the *x*-direction are also fixed. Occurring frictional effects and contact conditions in the plate guides are not taken into account. The displacement of 5 mm takes place at the right edge of the test plate with a displacement rate of 83.33 mm/s. For this purpose, all nodes of the individual layers are connected to a reference point via kinematic coupling constraint. The individual points thus carry out the same movement as the reference point. The two translational DOFs in *y*- and *z*-directions as well as all rotational DOFs of the reference point are fixed. Additionally, to ensure the stable time increment in the CAI model, a constant mass scaling factor of 10 is applied to the entire model.

3.3. Material properties

The total mass of the laminate is distributed between the plies and interfaces, where the mass density assigned to the top and bottom plies is 1.04 kg/m^3, the mass density assigned to the inner plies is 0.52 kg/m^3, and the mass density assigned to the cohesive zone element is 0.32 kg/m^3. Since the top and bottom plies are only connected to one interface, their mass density is two times higher than the inner plies so that the mass of each individual ply is equally distributed. However, Abaqus/Explicit relies on lumped mass matrices which keeps the mass distribution within each node remain unchanged, allowing the model to accurately capture the dynamic response of the laminate [5]. The material properties defining the constitutive behavior of the plies are given in Table 1. Four different modes that characterize composite material damage are generally fiber breaking under tension, fiber buckling and kinking under compression, matrix cracking under tension and shear loads, and crushing of matrix under compression and shear [18]. However, in Abaqus, the damage initiation criteria for fiber reinforced composites are based on Hashin's theory which considers four different damage initiation mechanisms such as fiber tension, fiber compression, matrix tension, and matrix compression [22]. These material properties are taken from the work of Springer [32].

Table 1. Material properties of plies describing the elastic behavior, the longitudinal strength (X), transverse strength (Y), and the fracture toughness along fiber direction (*x*, *y*) for both tension and compression as well as transverse and in-plane shear strengths, S^T and S^L, respectively [32].

Properties	Values
Young's modulus in x – direction, E_x	103.56 (GPa)
Young's modulus in y – direction, E_y	10.066 (GPa)
Young's modulus in z – direction, E_z	10.066 (GPa)
Shear modulus, $G_{xy} = G_{xz} = G_{yz}$	4.2058 (GPa)
Poisson's ratio, $\nu_{xy} = \nu_{xz}$	0.33
Poisson's ratio, ν_{yz}	0.2857
Longitudinal strength in tension, X^T	1541.5 (MPa)
Longitudinal strength in compression, X^C	1172.9 (MPa)
Transverse strength in tension, Y^T	62.742 (MPa)
Transverse strength in compression, Y^C	242.83 (MPa)
Transverse shear strength, S^T	115.83 (MPa)
In-plane shear strength, S^L	115.83 (MPa)
Fracture toughness in x-direction in tension, $\mathcal{G}_x^T$	89.8 (MPa$\sqrt{\text{mm}}$)
Fracture toughness in x-direction in compression, $\mathcal{G}_x^C$	78.3 (MPa$\sqrt{\text{mm}}$)
Fracture toughness in y-direction in tension, $\mathcal{G}_y^T$	0.2 (MPa$\sqrt{\text{mm}}$)
Fracture toughness in y-direction in compression, $\mathcal{G}_y^C$	0.8 (MPa$\sqrt{\text{mm}}$)

Table 2. The interface properties represented by cohesive zone element [32, 33].

Properties	Values
Initial stiffness in normal direction, K_{nn}	1.0 x 10^6 (N/mm^3)
Initial stiffness in shear direction, K_{ss}	1.0 x 10^6 (N/mm^3)
Initial stiffness in transverse direction, K_{tt}	1.0 x 10^6 (N/mm^3)
Inter-laminar strength in normal direction, t_n^0	60 (MPa)
Inter-laminar strength in shear direction, t_s^0	79.289 (MPa)
Inter-laminar strength in transverse direction, t_t^0	79.289 (MPa)
Critical energy release rates in normal direction, $\mathcal{G}_n^C$	0.133 (N/mm)
Critical energy release rates in shear direction, $\mathcal{G}_s^C$	0.46 (N/mm)
Critical energy release rates in transverse direction, $\mathcal{G}_t^C$	0.46 (N/mm)

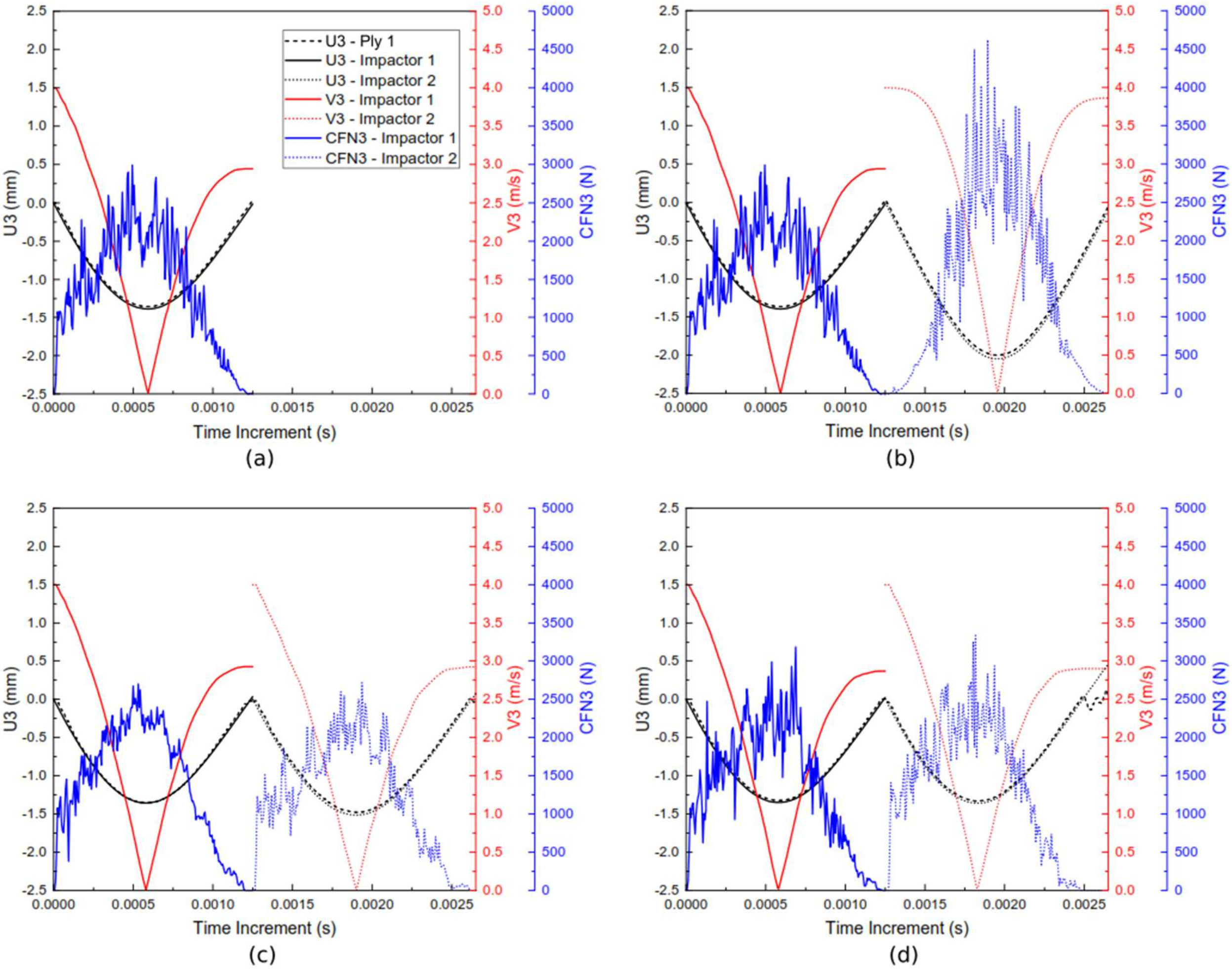

Fig. 3. The impactor response including displacement (U3), velocity magnitude (V3), and contact force (CFN3), as well as the displacement at the impact point of the ply 1 (top layer) on the laminated composites for (a) single, (b) double with impactor distance of 0 mm, (c) 10 mm, and (d) 20 mm of LVI events.

Table 2 lists the properties of the interface. To all cohesive zone elements, the same initial stiffness is assigned in normal, shear, and transverse direction of *Knn, Kss*, and *Ktt* independent to the geometrical thickness. The inter-laminar strengths, t_n^0, t_s^0, and t_t^0 are taken from [32]. The critical energy release rates, $\mathcal{G}_n$, $\mathcal{G}_s$, and $\mathcal{G}_t$are taken from values published in [33]. Additionally, for the impactor, the mass density of 59.7 kg/m^3 is defined to obtain a total impactor mass of 0.25 kg.

4. Results and Discussion

The following results are solely obtained by means of numerical simulations. All simulations are carried out using a cluster computer system of eight standard PC workstations. Each PC workstation provides 6 CPUs and thus in total, 48 CPUs are employed at 3.3 GHz.

4.1. Low-velocity impact

Figure 3 shows the impactor response including displacement, velocity magnitude, and contact force, as well as the displacement at the impact point of the top layer on the laminated composites for single and double 0 mm, 10 mm, and 20 mm of LVI events. The left and right curves represent the first impactor and second impactor, respectively. The black lines present the displacement of ply 1 (top layer), the first impactor, and the second impactor at the impact point shown as a dashed line, solid line, and dotted line, respectively. For the first LVI event, the top layer and the first impactor displacement are identical from the beginning until the impactor bounces back completely. This phenomenon demonstrates that no ply damage has occurred, implying that the ply stiffness does not significantly change while the delamination dominates the damage in laminated composites. In general, this phenomenon also occurs in the second LVI event. However, a slight fluctuation occurs in the double 20 mm case when the impactor is completely bounced back from the laminate. This fluctuation mainly occurs due to the vibration of the laminates after impact. Furthermore, the maximum displacement generated by the second impact event is significantly higher than the first impact event for the double 0 mm case because of the reduction in transverse shear stiffness due to delamination by the first impact. Additionally, the delamination due to the second impact is started to propagate when the displacement of the second impactor is higher than the maximum displacement of the first impactor.

The velocity magnitude of the first and second impactors is presented by the red lines, as shown in Fig. 3. When the impactor collides with the laminate, its velocity drops until it approaches zero, which represents the lowest point or maximum displacement of the impactor. At this point, the kinetic energy of the impactor is zero, but the recoverable strain energy of the laminates is at its maximum. As a result, the recoverable strain energy will be transferred back to the impactor, causing it to rebound. When the impactor bounces back, its velocity increases again. In terms of impact velocity, the second impactor for double 0 mm exhibits a different pattern. Even after colliding with the laminates, the impactor velocity is not reduced directly for a short period of time. This is due to the effect of deleted CZE and scaling the surface thickness of the plies by a factor of 0.8. This phenomenon does not occur in double 10 mm and 20 mm cases since the delamination has not been established in front of the second impact point.

The blue lines in Fig. 3 show the contact force between the impactor and the top layer of the laminate. In contrast to the impactor velocity, the contact force gradually increases until it reaches the delamination initiation threshold, at which point it begins to fluctuate due to delamination propagation. Furthermore, the contact force increases until the impactor reaches its maximum displacement and returns to zero when the impactor bounces back completely. The first impactor for double 10 mm and 20 mm exhibits a slightly different contact force pattern compared to the single impact event. This is due to the position of the impactor which is not exactly at the center of the laminates. Additionally, the second impactor for double 0 mm presents a high contact force compared to the first impactor. The loss of transverse shear stiffness of the laminates due to the first impact will increase the maximum displacement of the second impact. This corresponds to the increasing contact force between the impactor and the top layer of laminates.

Figure 4 presents the energy-time curves for the first and second impact events. Figure 4(a) illustrates the energy-time curve of a single impact event, along with the energy response of the first impact event for all configurations of the double impact event. Figures 4(b) and 4(c) depict the energy-time curves for the second impact event in the double 0 mm and 10 mm cases, respectively. The energy-time curves for the second impact event in the double 20 mm case are not included, as the delamination caused by the second impact is independent of the first. In other words, the energy analysis for the second impact event in this configuration is identical to that of the first.

As shown in Fig. 4(a), the kinetic energy of the impactor is converted into internal energy or total strain energy, which is further divided into recoverable strain energy and damage dissipation energy [34]. When the impactor reaches maximum displacement, its kinetic energy drops to zero. The laminated composite then releases the recoverable strain energy back to the impactor, causing it to rebound and leaving the laminate in a swinging motion. However, as described in Section 3.2, changes in the boundary conditions eventually dampen this motion.

Figure 4(b) shows that in the double 0 mm case, the damage dissipation energy for the second impact is significantly lower than that of the first. This reduction occurs because delamination has already been initiated in the laminate, meaning that delamination propagation only begins when the displacement of the second impactor exceeds the maximum displacement of the first impactor. In contrast, the recoverable strain energy of the second impactor, upon rebounding, is higher than that of the first impactor.

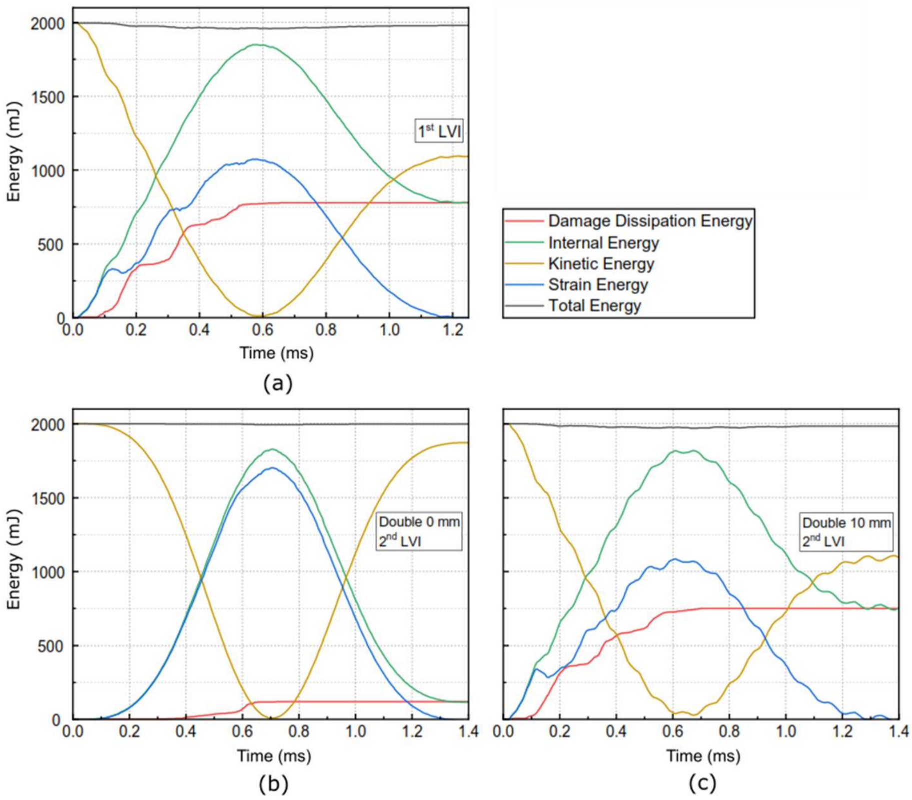

Fig. 4. Energy-time curves for the (a) first and (b) second impact events of the double 0 mm, as well as (c) the second impact event of the double 10 mm.

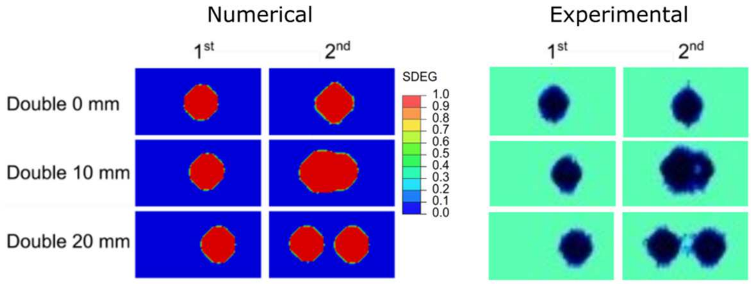

Fig. 5. The stiffness degradation of the interface a of the laminate for the first and second impact events for all configurations.

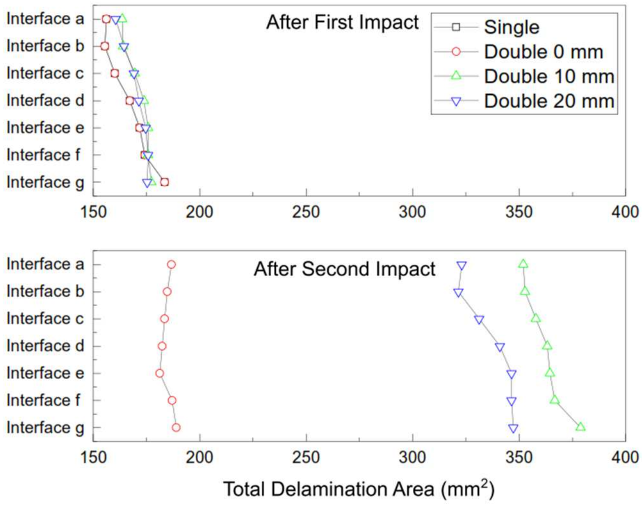

Fig. 6. Delamination area after the first and the second impact events at every interface for all configurations.

Figure 4(c) illustrates the fluctuations in kinetic, internal, and strain energies during the second impact event. These fluctuations arise from the interaction between the delamination created by the first impact and the initiation and propagation of delamination during the second impact loading. Since Abaqus/Explicit is used, the total energy should ideally remain constant throughout the impact event. However, a slight reduction in total energy is observed in these configurations. This energy loss occurs due to element deletion in the cohesive zone elements (CZEs) when full damage is reached.

Overall, the energy dissipation mechanisms vary between impact positions due to several factors, including material anisotropy, boundary conditions, and delamination interaction. Material anisotropy influences energy absorption and redistribution, as different fiber orientations affect how strain energy is stored and released. Additionally, boundary conditions, such as laminate constraints and surface interactions, impact the recoverable strain energy and the rebound behavior of the impactor. In the double 0 mm case, pre-existing delamination reduces stiffness, leading to lower damage dissipation energy in the second impact. Conversely, in the double 10 mm case, delamination interaction enhances propagation, resulting in increased energy dissipation.

The delamination damage state is represented by the stiffness degradation (SDEG) of the CZEs. When the SDEG of a CZE is equal to one, it is indicated that the CZE is fully damaged and is deleted in the simulation. The SDEG of the interface a of the laminate for all configurations is presented in Fig. 5. Figure 5 shows that the delamination area due to the first impact has almost the same shape, but after the second impact, the shape of the delamination area is different. This difference occurs when the delamination due to the first and second impacts interfere, interact, and do not interact with each other as shown in the cases of double 0 mm, double 10 mm, and double 20 mm, respectively. These delamination interference mechanisms are consistent with the experimental findings of Liao et al. [13]. Liao et al. stated that the two impacts can be categorized as either "noninterfering" or "interfering" based on the extent of separation between the damage regions caused by two impact positions [13]. Physically, the first low-velocity impact directly affects the laminate's deflection, stiffness, and delamination, leading to greater displacement during the second low-velocity impact, which correlates with the phenomena shown in Fig. 3. [35–37].

The delamination area generated by the first and second impact event at every interface is illustrated in Fig. 6. The delamination area on the double 10 mm and double 20 mm after the first impact event differs slightly from that of the single and the Double 0 mm. This phenomenon is caused by the fact that the impactor position of double 10 mm and double 20 mm cases is not at the center of the laminate. Overall, the delamination area after the first impact has a conical type damage from interface a to interface g, which conforms to the concept of delamination damage in a laminated composite structure under LVI [18, 38]. The delamination area at double 0 mm after the second impact event is increased slightly, while the delamination area at all interfaces remains similar. In comparison to other configurations, the delamination area of double 10 mm after the second impact event is the largest. This phenomenon occurs because the delamination propagation during the second impact event interacts with the established delamination. Consequently, the established delamination is triggered to propagate. Furthermore, the delamination area of double 20 mm after the second impact event is about two times after the first impact event. It is due to the fact that delamination is not interacting with each other as shown in Fig. 5.

4.2. Compression after Impact

Compression tests are simulated for all impacted samples along with the unimpacted sample (CUS) to determine the compressive strength of the laminated composites, as illustrated in Fig. 7. It is observed that the compressive strength of the unimpacted sample is reduced by approximately 50% when the CAI is applied. This is consistent with research by Richardson and Wisheart [39], who found that very small damage like barely visible impact damage (BVID) can reduce residual strength by up to 50%.

Table 3. Computational time comparison of LVI and CAI simulations.

	Element Number	DOFs	CPU Number	CPU Time (hrs)		
				LVI	CAI	Total
Present study	561,435	1,448,580	48	1	2.5	3.5
Gonzalez et al. [40]	-	-	24	-	-	288
Lin and Wass [41]	-	1,431,852	72	3.4	2.7	6.1
Zhang et al. [42]	180,000	-	48	-	-	9

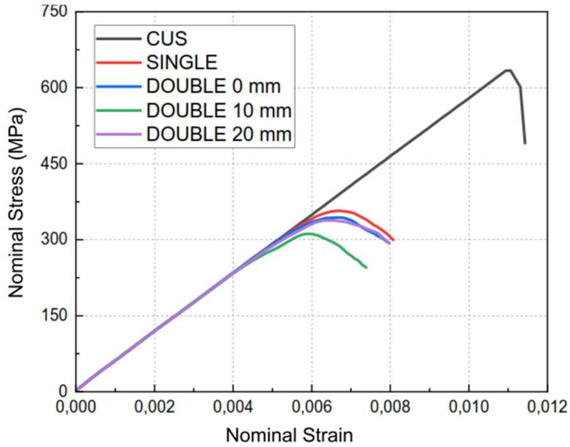

Fig. 7. Predictions of the compressive strength of all impacted laminated composite plates along with the unimpacted laminated composite plate.

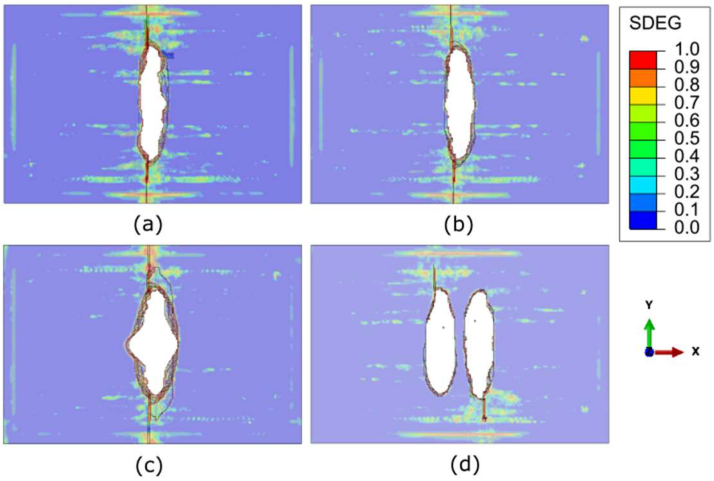

Fig. 8. The stiffness degradation of the CZEs after compression load of (a) single, (b) double 0 mm, (c) double 10 mm, and (d) double 20 mm at the interface a.

For the single impact, the compressive strength is reduced from 634 MPa to 357 MPa. For double 0 mm, double 10 mm, and double 20 mm, the compressive strength is reduced from 634 MPa to 344 MPa, 311 MPa, and 338 MPa respectively. The compressive strength of the laminates is significantly affected by the delamination area for the studied configurations. Figure 8 presents the stiffness degradation distribution of the CZEs where the fully damage CZEs are deleted (white regions at the center of the laminate). Figure 8 also shows that all configurations exhibit the same failure mode, namely crack propagation through the impacted location, delamination propagation, and specimen crushing. Hence, the impact indentation causes a stress concentration effect in the specimens. This behavior is consistent with the studies of Anuse et al. [18].

As brief information about the efficiency of the conventional shell-based ply-level modeling strategy in combination with finite thickness CZEs, a single LVI and CAI and its comparison with the previous study are summarized in Table 3. Table 3 lists that the present study configuration by implementing ply-based modeling strategy has the lowest computational time. However, generally, computation time is dependent on several factors including impact energy, size of the model, and element size.

5. Conclusions

The mechanical response, damage mechanisms, and compressive strength of laminated composites were comprehensively studied by performing single and double LVI and CAI by the means of the Finite Element Method. From the numerical predictions, it can be concluded that different numbers of impact events as well as the impact position will lead to different delamination behavior, especially, if the delamination interact with each other. Moreover, the LVI loading reduced the compressive strength of the laminated composites by approximately 50% for all configurations. Finally, the use of ply-level modeling based on shell elements in combination with finite geometrical thickness of cohesive zone elements for predicting the impact response and the compressive strength of laminated composite structures provided high computational efficiency.

Author Contributions

K. Anam planned the scheme, initiated the project, and conducted the numerical experiments; M. Todt reviewed and analyzed the LVI event; H.E. Pettermann reviewed and analyzed the CAI event. The manuscript was written through the contribution of all authors. All authors discussed the results, reviewed, and approved the final version of the manuscript.

Acknowledgments

The Indonesian Ministry of Higher Education, Science, and Technology (KEMDIKTISAINTEK) and Österreichs Agentur für Bildung und Internationalisierung (OeAD-GmbH) in collaboration with ASEAN European Academic University Network (ASEA-UNINET) are gratefully acknowledged for sponsoring KA under Indonesia-Austria Scholarship Programme.

Conflict of Interest

The authors declared no potential conflicts of interest concerning the research, authorship, and publication of this article.

Funding

The authors received no financial support for the research, authorship, and publication of this article.

Data Availability Statements

The datasets generated and/or analyzed during the current study are available from the corresponding author on reasonable request.

Nomenclature

B	Mode-mixity
E_i	Young's modulus (i = x, y, z) [GPa]
G_i	Shear modulus (i = xy, xz, yz) [GPa]
$\mathcal{G}_i$	Strain energy release rate (i = n, s, t) [N/mm]
$\mathcal{G}_i^C$	Critical strain energy release rate (i = n, s, t) [N/mm]
$\mathcal{G}_x^j$	Fracture toughness in x-direction (i = T, C) [MPa$\sqrt{\text{mm}}$]
$\mathcal{G}_y^j$	Fracture toughness in y-direction (j = T, C) [MPa$\sqrt{\text{mm}}$]
K_i	Initial stiffness (i = nn, ss, tt) [N/mm^3]
S^L	In-plane shear strength [MPa]
S^T	Transverse shear strength [MPa]
t_i^0	Inter-laminar strength (i = n, s, t) [MPa]
t_i	Traction (i = n, s, t) [MPa]
X^i	Longitudinal strength (i = T, C) [MPa]
Y^i	Transverse strength (i = T, C) [MPa]
δ_i	Separation (i = n, s, t) [mm]
η	Cohesive parameter
ν_i	Poisson's ratio (i = xy, xz, yz)

References

[1] Anam, K., Todt, M., Pettermann, H.E. An efficient ply-level based modeling strategy for predicting delamination behavior in laminated composites, *Journal of Applied and Computational Mechanics*, 10, 2024, 652-658.
[2] Sasikumara, A., Triasa, D., Costa, J., Blanco, N., Orr, J., Linde, P. Effect of ply thickness and ply level hybridization on the compression after impact strength of thin laminates, *Composites Part A: Applied Science and Manufacturing*, 121, 2019, 232–243.
[3] Aymerich, F., Dore, F., Priolo, P. Simulation of multiple delaminations in impacted cross-ply laminates using a finite element model based on cohesive interface elements, *Composites Science and Technology*, 69, 2009, 1699–1709.
[4] Feng, D., Aymerich, F. Modeling and simulation of damage and failure in large composite components subjected to impact loads, *Composite Structures*, 108, 2014, 161–171.
[5] Schwab, M., Todt, M., Wolfahrt, M., Pettermann, H.E. Failure mechanism-based modeling of impact on fabric reinforced composite laminates based on shell elements, *Composites Science and Technology*, 128, 2016, 131–137.
[6] Schwab, M., Pettermann, H.E. Modeling and simulation of damage and failure in large composite components subjected to impact loads, *Composite Structures*, 158, 2016, 208–216.
[7] Schoeppner, G.A., Abrate, S. Delamination threshold loads for low-velocity impact on composite laminates, *Composites Part A: Applied Science and Manufacturing*, 31, 2000, 903–915.
[8] Sjögren, A., Krasnikovs, A., Varna, J. Experimental determination of elastic properties of impact damage in carbon fibre/epoxy laminates, *Composites Part A: Applied Science and Manufacturing*, 32, 2001, 1237–1242.
[9] Vachon, P.L., Brailovski, V., Terriault, P. Prediction of the propagation of impact-induced delamination in carbon/epoxy laminates, *Composite Structures*, 95, 2013, 227–235.
[10] Vaidya, U.K. Impact response of laminated and sandwich composites, Impact Engineering of Composite Structures, *CISM International Centre for Mechanical Sciences*, 526, 2011, 97–191.
[11] Sevkat, E., Liaw, B., Delale, F., Raju, B.B. Effect of repeated impacts on the response of plain-woven hybrid composites, *Composites Part B: Engineering*, 41, 2010, 403–413.
[12] Ling, Z., Ling, G.K., Gang, L.Y., Yu, T.X., Weng, Z.Q. Experimental study on the dynamic behaviour of aluminium foam sandwich plates under single and repeated impacts at low temperature, *International Journal of Impact Engineering*, 114, 2018, 123–132.
[13] Liao, B.B., Wang, P.D., Zheng, J.Y., Cao, X.F., Li, Y., Ma, Q.J., Tao, R., Fang, D.N. Effect of double impact positions on the low-velocity impact behaviors and damage interference mechanism for composite laminates, *Composites Part A: Applied Science and Manufacturing*, 136, 2020, 105964.
[14] Bogenfeld, R., Kreikemeier, J., Wille, T. Review and benchmark study on the analysis of low-velocity impact on composite laminates, *Engineering Failure Analysis*, 86, 2018, 72–99.
[15] Saleh, M.N., El-Dessouky, H.M., Saeedifar, M., Freitas, S.T., Scaife, R.J., Zarouchas, D. Compression after multiple low-velocity impacts of NCF, 2D and 3D woven composites, *Composites Part A: Applied Science and Manufacturing*, 125, 2019, 105576.
[16] Shah, S.Z.H., Karuppanan, S., Megat-Yusoff, P.S.M., Sajid, Z. Impact resistance and damage tolerance of fiber reinforced composites: a review, *Composite Structures*, 217, 2019, 100–121.
[17] Andrew, J.J., Arumugam, V., Saravanakumar, K., Dhakal, H.N., Santulli, C. Compression after impact strength of repaired GFRP composite laminates under repeated impact loading, *Composite Structures*, 133, 2015, 911–920.
[18] Anuse, V.S., Shankar, K., Velmurugan, R., Ha, S.K. Compression-after-impact analysis of carbon fiber reinforced composite laminate with different ply orientation sequences, *International Journal of Impact Engineering*, 2022, 104277.
[19] Ceglar, T., Schwab, M., Pettermann, H.E. DCB and ENF multi-scale simulations, *6th ECCOMAS Thematic Conference on the Mechanical Response of Composites: COMPOSITES*, 2017, 13–23.
[20] ASTM Standard, D7136/D7136M Standard Test Method for Measuring the Damage Resistance of a Fiber-Reinforced Polymer Matrix Composite to a

Drop-Weight Impact Event, ASTM International, 2012, 1–16.
[21] ASTM Standard, D7137/D7137M Standard Test Method for Compressive Residual Strength Properties of Damaged Polymer Matrix Composite Plates, ASTM International, 2012, 1–16.
[22] Dassault Systemes Simulia Corp. Abaqus Analysis User's Guide, Release 2020, 2020.
[23] Hashin, Z. Failure criteria for unidirectional fiber composites, *Journal of Applied Mechanics*, 47, 1980, 329–334.
[24] Hashin, Z., Rotem, A. A fatigue failure criterion for fiber reinforced materials, *Journal of Composite Materials*, 7, 1973, 448–464.
[25] Matzenmiller, A., Lubliner, J., Taylor, R.L. A constitutive model for anisotropic damage in fiber-composites, *Mechanics of Materials*, 20, 1995, 125–152.
[26] Camanho, P.P., Davila, C.G. Finite elements for the simulation of delamination in composite materials, *NASA/TM-2002–211737*, 2002, 1–37.
[27] Camanho, P.P., Davila, C.G., Moura, M.F.D. Numerical simulation of mixed-mode progressive delamination in composite materials, *Journal of Composite Materials*, 37, 2003, 1415–1438.
[28] Benzeggagh, M.L., Kenane, M. Measurement of mixed-mode delamination fracture toughness of unidirectional glass/epoxy composites with mixed-mode bending apparatus, *Composite Science and Technology*, 56, 1968, 439–449.
[29] Padaki, N.V., Alagirusamy, R. Low-velocity impact behavior of textile reinforced composites, *Indian Journal of Fibre and Textile Research*, 33, 2008, 189–202.
[30] Mishra, A., Naik, N.K. Failure initiation in composite structures under low-velocity impact: Analytical studies, *Composite Structures*, 92, 2010, 436–444.
[31] Abrate, S. Impact on laminated composite materials, Applied Mechanics Review, 44, 1991, 155–190.
[32] Springer, M. *Nichtlineare Finite Elemente Simulation der Schädigungsmechanismen sowie der Resttragfähigkeit von Schlagbeanspruchten Kohlenstofffaser-Epoxidharz-Verbunden*, Master Thesis, TU Wien, ILSB, Vienna, Austria, 2014.
[33] Hadavinia, H., Ghasemnejad, H. Effects of mode-I and mode-II interlaminar fracture toughness on the energy absorption of CFRP twill/weave composite box sections, *Composite Structures*, 89, 2009, 303–314.
[34] Sevkat, E., Liaw, B., Delale, F., Raju, B.B. Drop-weight impact of plain-woven hybrid glass–graphite/toughened epoxy composites, *Composites Part A*, 40, 2009, 1090–1110.
[35] Li, Y.P., She, G.L. Nonlinear dynamic response of porous graphene platelets reinforced plates subjected to moving load considering initial geometrical imperfection, *Journal of Vibration Engineering & Technologies*, 13, 2025, 17.
[36] She, G.L., Ma, Z.S., Li, C., Eltaher, M.A. Geometrically nonlinear transient response of graphene platelets reinforced metal foams arbitrary quadrilateral plates under blast load, *Thin-Walled Structures*, 210, 2025, 113018.
[37] Fan, Y.H., She, G.L. Nonlinear transient response of graphene platelets reinforced metal foams beam considering initial geometrical imperfection and viscoelastic elastic foundation, *Computers and Concrete*, 35, 2025, 59–70.
[38] Bouvet, C., Rivallant, S., Barrau, J.J. Low-velocity impact modeling in composite laminates capturing permanent indentation, *Composites Science and Technology*, 72, 2012, 1977–1988.
[39] Richardson, M.O.W., Wisheart, M.J. Review of low-velocity impact properties of composite materials, *Composites Part A: Applied Science and Manufacturing*, 27, 1996, 1123–1131.
[40] González, E., Maimí, P., Camanho, P., Turon, A., Mayugo, J. Simulation of drop-weight impact and compression after impact tests on composite laminates, *Composite Structures*, 94, 2012, 3364–3378.
[41] Lin, S., Waas, A.M. Accelerating computational analyses of low-velocity impact and compression after impact of laminated composite materials, *Composite Structures*, 260, 2021, 113456.
[42] Zhang, D., Zheng, X., Zhou, J., Zhang, W. Bridging the low-velocity impact energy versus impact damage and residual compression strength for composite laminates, *Journal of Reinforced Plastics and Composites*, 40, 2021, 378–390.

ORCID iD

Khairul Anam https://orcid.org/0000-0002-8588-9528
Melanie Todt https://orcid.org/0000-0002-5599-6373
Heinz E. Pettermann https://orcid.org/0000-0001-7162-5989

How to cite this article: Anam K., Todt M., Pettermann H.E. Numerical Investigation of Double Low-Velocity Impact and Post-Impact Compression Behavior in Laminated Composites, *J. Appl. Comput. Mech.*, 12(1), 2026, 21–30. https://doi.org/10.22055/jacm.2025.48157.5019